Full Length Article

Ductile Co-based bulk metallic glass with superhigh strength and excellent soft magnetic properties induced by modulation of structural heterogeneity

Qianqian Wang[a], Jing Zhou[a], Qiaoshi Zeng[a], Genlei Zhang[a], Kuibo Yin[b], Tao Liang[a], Weiming Yang[c], Mihai Stoica[d], Litao Sun[b], Baolong Shen[a,c,∗]

[a] School of Materials Science and Engineering, Jiangsu Key Laboratory for Advanced Metallic Materials, Southeast University, Nanjing 211189, China
[b] SEU-FEI Nano-Pico Center, Key Laboratory of MEMS of Ministry of Education, Southeast University, Nanjing 210096, China
[c] Institute of Massive Amorphous Metal Science, China University of Mining and Technology, Xuzhou 221116, China
[d] Laboratory of Metal Physics and Technology, Department of Materials, ETH Zurich, 8093 Zurich, Switzerland

ARTICLE INFO

ABSTRACT

The development of Co-based bulk metallic glasses (BMGs) with satisfying comprehensive properties, including large glass-forming ability, high strength, large plasticity and excellent soft magnetic properties, is in high need for applications as structural and functional materials. A $(Co_{0.7}Fe_{0.2}Ni_{0.1})_{67.7}B_{21.9}Si_{5.1}Nb_5Cu_{0.3}$ BMG with a record large plasticity of 5.5%, a high fracture strength of 4770 MPa, and a large critical diameter of 3.5 mm is successfully developed. This BMG also shows good soft magnetic properties, i.e. low coercivity (H_c) of 1.33 A/m and higher saturation magnetization (B_s) of 0.60 T. The enhanced strength and plasticity, as well as high B_s of this BMG, are all attributed to the minor addition of Cu in $(Co_{0.7}Fe_{0.2}Ni_{0.1})_{68-x}B_{21.9}Si_{5.1}Nb_5Cu_x$ ($x = 0$, 0.1, 0.3, 0.5 and 0.7 at.%) system. The reduced average atomic spacing in the BMG, which comes from the squeezed spacing between Co, Fe, Ni and Nb atoms with proper addition of Cu, results in the improvement of fracture strength and B_s. The atomic-scale structural heterogeneity with the formation of crystal-like order structures is induced in the amorphous matrix, and thus the plasticity of $(Co_{0.7}Fe_{0.2}Ni_{0.1})_{67.7}B_{21.9}Si_{5.1}Nb_5Cu_{0.3}$ BMG increases in spite of the decreased average atomic spacing.

1. Introduction

Co-based metallic glasses are promising functional materials for engineering applications due to their excellent magnetic properties, i.e., high effective permeability and low coercivity (H_c) [1–5]. In 2003, the first Co-based bulk metallic glass (BMG) with a composition of $Co_{43}Fe_{20}Ta_{5.5}B_{31.5}$ was fabricated by copper mold casting method. The resulted cylindrical rods have a critical diameter (D_C) of 2 mm [6]. The surprisingly high fracture strength of 5185 MPa for this Co-based BMG attracted considerable research attentions, and a large number of Co-based BMGs have been prepared since then [7–13]. By proper adjustment of the Co/Ta ratio, the fracture strength of the ternary $Co_{55}Ta_{10}B_{35}$ BMG reached 6020 MPa, which is the largest value among all the BMGs [14]. After that, the successful preparation of $Co_{42}Cu_1Fe_{20}Ta_{5.5}B_{26.5}Si_5$ BMG improved the D_C of Co-based BMGs up to 6 mm [15]. However, the structural and functional applications of Co-based BMGs are limited by their poor room-temperature plasticity, as the plastic strain of most Co-based BMGs is less than 2%. The poor plastic deformation ability of the Co-based BMGs not only makes the manufacturing processes difficult,

such as folding, but also reduces their reliability as structural materials. For example, the plastic strain of the $Co_{55}Ta_{10}B_{35}$ BMG that mentioned above is only 0.5% [14], which may result in catastrophic failure under loading.

Introducing structural heterogeneity in the amorphous matrix by adding elements that either have a large Poisson's ratio or positive mixing enthalpy with the major elements has been widely used to improve the plasticity of BMGs [16,17]. Some efforts using this method have been devoted to improve the limited room-temperature plasticity of Co-based BMGs [18–20], however, none of these Co-based BMGs shows satisfying comprehensive properties, i.e. large plasticity, high strength and large glass-forming ability (GFA). For example, by substituting Ta with Nb, which has a large Poisson's ratio of 0.4, the structural heterogeneity with the formed medium-range order clusters of 1–2 nm scale is induced in the ternary $Co_{61}Nb_8B_{31}$ BMG, leading to the improvement of their plastic strain up to 5.0% [21,22]. Unfortunately, the D_C of $Co_{61}Nb_8B_{31}$ BMG is only 1.5 mm. Furthermore, for the CoFeBSiNb BMG systems that have a large D_C up to 5.5 mm, improvement of the plasticity is achieved by the increased structural heterogeneity with the formation of Co(Fe)-rich

clusters by minor addition of Cu, which has large positive mixing enthalpy with Co/Fe elements [20,23]. However, the largest plastic strain obtained in the CoFeBSiNb BMG systems is only 2.5%. Thus, the development of Co-based BMGs with good comprehensive properties remains a big challenge.

It was reported that modulation of the structural heterogeneity is effective in improving not only the plasticity but also the fracture strength and GFA of CuZr-based BMGs. In the CuZrAl BMG, by addition of Y, which has a positive mixing enthalpy with Zr [24], the plasticity and GFA of the BMG was improved simultaneously because of the introduction of atomic-scale heterogeneity [25]. Comparative studies on the $Cu_{50}Zr_{50}$ and $Cu_{47.5}Zr_{47.5}Al_5$ amorphous alloys showed that the minor addition of Al led to higher inhomogeneity in the amorphous matrix by the formation of more icosahedral medium-range orders, and resulted in the increased yield strength and GFA; moreover, the even distribution of these icosahedra also improved the plasticity [26]. Simultaneous improvement in plasticity and strength was also achieved in $Cu_{46}Zr_{46}Ag_8$ BMG by introducing atomic-scale heterogeneities as Ag and Cu have a positive mixing enthalpy [27]. Inspired by these works, we aim to develop Co-based BMGs with large GFA, high strength and large room-temperature plasticity by substantially increasing the degree of their atomic-scale structural heterogeneity. Also, the soft magnetic properties of the Co-based BMGs should not be deteriorated.

In this work, we started from the previously reported $(Co_{0.7}Fe_{0.3})_{68}B_{21.9}Si_{5.1}Nb_5$ BMG, which has a large GFA of 5.5 mm but no room-temperature plasticity [10], and took $(Co_{0.7}Fe_{0.2}Ni_{0.1})_{68}B_{21.9}Si_{5.1}Nb_5$ as the base alloy by substituting some Fe with Ni to introduce a certain degree of structural heterogeneity, as the mixing enthalpies of Co-Ni and Fe-Ni pairs are both close to 0, and Ni has a large Poisson's ratio [28–30]. In order to further increase the structural heterogeneity, different amount of Cu was then added in the base alloy to prepare $(Co_{0.7}Fe_{0.2}Ni_{0.1})_{68-x}B_{21.9}Si_{5.1}Nb_5Cu_x$ (x = 0, 0.1, 0.3, 0.5 and 0.7 at.%) BMGs. A novel $(Co_{0.7}Fe_{0.2}Ni_{0.1})_{67.7}B_{21.9}Si_{5.1}Nb_5Cu_{0.3}$ BMG with not only an improved plasticity of 5.5%, but also an increased fracture strength of 4770 MPa was successfully prepared. The enhanced strength is supposed to originate from the reduced atomic spacing in the alloy, as revealed by synchrotron radiation X-ray diffraction (XRD). The improved plasticity came from the structural heterogeneity induced by Cu addition, which was verified by spherical aberration corrected high-resolution transmission electron microscope (HRTEM).

2. Experimental

2.1. Sample preparation

Multicomponent Co-based alloy ingots with nominal compositions of $(Co_{0.7}Fe_{0.2}Ni_{0.1})_{68-x}B_{21.9}Si_{5.1}Nb_5Cu_x$ (x = 0, 0.1, 0.3, 0.5 and 0.7 at.%) were prepared by arc melting mixtures of Co (99.99%), Fe (99.99%), Ni (99.99%), B (99.999%), Si (99.99%), Nb (99.95%), and Cu (99.995%) in a high purity argon atmosphere. Ribbons with a thickness of 30 μm and a width of 1.2 mm were produced by the single roller melt-spinning method. BMGs as cylindrical rods with different diameters were fabricated by the copper mold injection casting method. The length of the glassy rods is between 20–50 mm long when the diameter is 1 mm; and the glassy rods with a diameter more than 1 mm are usually 50–80 mm long.

2.2. Mechanical and magnetic property tests

Mechanical properties including fracture strength and plastic strain were measured by compression tests at room temperature with a Sans 5305 electromechanical testing machine at a strain rate of 5×10^{-4} s^{-1}. The gauge size of bulk glassy rods for compression tests was 1 mm in diameter and 2 mm in length. The saturation magnetization (B_s) of glassy ribbons was measured with a vibrating sample magnetometer (VSM, Lake Shore 7410) under an applied field of 800 kA/m. The H_c

of glassy ribbons with the length of 70 mm was measured using a DC B-H loop tracer (RIKEN BHS-40) under a maximum field of 800 A/m. All of the samples for magnetic property measurements were annealed for 300 s at specific temperatures (50 K less than the glass transition temperature) for structural relaxation. The glass transition temperatures (T_g) of the glassy ribbons were measured by differential scanning calorimeter (DSC, NETZSCH 404F3) at a heating rate of 0.67 K/s. The measured T_g values of $(Co_{0.7}Fe_{0.2}Ni_{0.1})_{68-x}B_{21.9}Si_{5.1}Nb_5Cu_x$ (x = 0, 0.1, 0.3, 0.5 and 0.7 at.%) glassy ribbons are 843, 838, 833, 836 and 842 K, respectively. The T_g value of each sample is the averaged result of three tests, and the errors of T_g for all the samples are within ±3 K.

2.3. Microstructural characterization

The amorphous nature of the as-cast alloys was identified by X-ray diffraction (XRD, Bruker D8 Discover) with Cu-$K\alpha$ radiation. The deformed and fracture surfaces of the glassy rods after compression tests were examined by scanning electron microscope (SEM, FEI Sirion 200). HRTEM analyses of the bulk glassy rods were carried out on a spherical aberration-corrected FEI Titan 80–300 transmission electronic microscope. The samples for HRTEM analyses were obtained from the 1 mm cylindrical rods (similar as the ones used for mechanical property tests) by ion milling method (Gatan Inc., PIPS-M691) under liquid nitrogen cooling condition, which keeps the temperature of samples below 193 K during milling process to avoid the negative impact of heating from the beam [31,32]. The melt-spun ribbons were analyzed using synchrotron radiation XRD with a wavelength of 0.1174 Å at beam line 11-IDC at the Advanced Photon Source, Argonne National Laboratory, USA. The two dimensional diffraction images were recorded using a Perkin–Elmer amorphous silicon detector and integrated to one dimensional XRD pattern by the program Fit2D [33]. Then, the data were normalized to get the total structural factor $S(Q)$ and corresponding reduced pair distribution functions $G(r)$ through the software PDFgetX2 [34,35].

3. Results

3.1. Mechanical properties

Cylindrical rods of $(Co_{0.7}Fe_{0.2}Ni_{0.1})_{68-x}B_{21.9}Si_{5.1}Nb_5Cu_x$ (x = 0, 0.1, 0.3, 0.5 and 0.7 at.%) with varied diameters were produced and examined under XRD to evaluate the largest glassy rods that can be produced without crystallization, in another word, the D_C of the BMGs. The larger D_C, the better GFA of BMG. The D_C of $(Co_{0.7}Fe_{0.2}Ni_{0.1})_{68-x}B_{21.9}Si_{5.1}Nb_5Cu_x$ (x = 0, 0.1, 0.3, 0.5 and 0.7 at.%) glassy rods are 5, 4, 3.5, 3 and 2 mm, respectively, indicating the large GFA of this alloy system.

The compressive stress-strain curves of $(Co_{0.7}Fe_{0.2}Ni_{0.1})_{68-x}B_{21.9}Si_{5.1}Nb_5Cu_x$ (x = 0, 0.1, 0.3, 0.5 and 0.7 at.%) BMGs are shown in Fig. 1. The amorphous nature of the samples used for compressive tests were confirmed by XRD. All of these alloys have similar elastic strain of about 2%. When x = 0, 0.1, 0.3, 0.5 and 0.7, the fracture strength of the samples are 4275, 4475, 4770, 4410 and 4340 MPa, respectively, while the plastic strain are 1.8, 3.4, 5.5, 2.0 and 0.8%, respectively. The Critical diameters, fracture strength and plastic strain of the BMGs are summarized in Table 1. According to our previous work, without Ni or Cu addition, the compressive plastic strain of $(Co_{0.7}Fe_{0.3})_{68}B_{21.9}Si_{5.1}Nb_5$ BMG is only 0.8% [20]. Therefore, the substitution of 1/3 Fe with Ni increases the plastic strain of the BMG. Moreover, with the increase of Cu addition, both the fracture strength and plastic strain firstly increase and then decrease, reaching the highest value in $(Co_{0.7}Fe_{0.2}Ni_{0.1})_{67.7}B_{21.9}Si_{5.1}Nb_5Cu_{0.3}$ BMG.

The GFA, strength and plastic strain of the $(Co_{0.7}Fe_{0.2}Ni_{0.1})_{67.7}B_{21.9}Si_{5.1}Nb_5Cu_{0.3}$ BMG are compared with other Co-based BMGs that have been reported, as shown in Fig. 2. The Co-based BMGs can be categorized into three groups according to their GFA and mechanical properties: (I) CoTaB(Fe)(Mo)(Si)(Cu), (II) CoAB (A=Nb or Ta), and
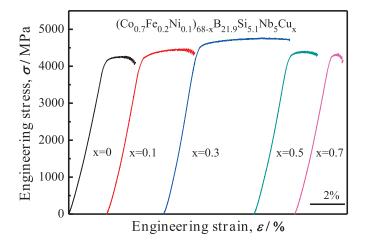
Fig. 1. Compressive stress-strain curves of $(Co_{0.7}Fe_{0.2}Ni_{0.1})_{68-x}B_{21.9}Si_{5.1}Nb_5Cu_x$ (x = 0, 0.1, 0.3, 0.5 and 0.7 at.%) glassy rods with diameters of 1 mm.
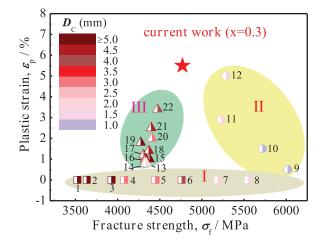

Fig. 2. Comparison of D_C, fracture strength and plastic strain for Co-based BMGs categorized into three groups: (I) CoTaB(Fe)(Mo)(Si)(Cu) (grey area), (II) CoMB (M=Nb or Ta) (yellow area), and (III) CoFeBSiNb(Cu)(Ni) (green area). Group I: 1. $Co_{41.5}Cu_{1.5}Fe_{20}Ta_{5.5}B_{26.5}Si_5$ [15], 2. $Co_{42.5}Cu_{0.5}Fe_{20}Ta_{5.5}B_{26.5}Si_5$ [15], 3. $Co_{42}Cu_1Fe_{20}Ta_{5.5}B_{26.5}Si_5$ [15], 4. $Co_{43}Fe_{20}Ta_{5.5}B_{26.5}Si_5$ [15], 5. $[(Co_{0.535}Fe_{0.1}Ta_{0.055}B_{0.31})_{0.98}Mo_{0.02}]_{98}Si_2$ [36], 6. $Co_{62.2}B_{26.9}Si_{6.9}Ta_4$ [37], 7. $Co_{43}Fe_{20}Ta_{5.5}B_{31.5}$ [6,7], 8. $(Co_{0.535}Fe_{0.1}Ta_{0.055}B_{0.31})_{98}Mo_2$ [36]; Group II: 9. $Co_{55}Ta_{10}B_{35}$ [14], 10. $Co_{59}Ta_6B_{35}$ [14], 11. $Co_{62}Nb_8B_{30}$ [21], 12. $Co_{61}Nb_8B_{31}$ [21,22]; Group III: 13. $(Co_{0.7}Fe_{0.2}Ni_{0.1})_{67.3}B_{21.9}Si_{5.1}Nb_5Cu_{0.7}$, 14. $[(Co_{0.7}Fe_{0.3})_{0.68}B_{0.219}Si_{0.051}Nb_{0.05}]_{99.1}Cu_{0.9}$ [20], 15. $(Co_{0.7}Fe_{0.3})_{68}B_{21.9}Si_{5.1}Nb_5$ [10], 16. $[(Co_{0.7}Fe_{0.3})_{0.68}B_{0.219}Si_{0.051}Nb_{0.05}]_{99.9}Cu_{0.1}$ [20], 17. $[(Co_{0.7}Fe_{0.3})_{0.68}B_{0.219}Si_{0.051}Nb_{0.05}]_{99.3}Cu_{0.7}$ [20], 18. $[(Co_{0.7}Fe_{0.3})_{0.68}B_{0.219}Si_{0.051}Nb_{0.05}]_{99.7}Cu_{0.3}$ [20], 19. $(Co_{0.7}Fe_{0.2}Ni_{0.1})_{68}B_{21.9}Si_{5.1}Nb_5$, 20. $(Co_{0.7}Fe_{0.2}Ni_{0.1})_{67.5}B_{21.9}Si_{5.1}Nb_5Cu_{0.5}$, 21. $[(Co_{0.7}Fe_{0.3})_{0.68}B_{0.219}Si_{0.051}Nb_{0.05}]_{99.5}Cu_{0.5}$ [20], 22. $(Co_{0.7}Fe_{0.2}Ni_{0.1})_{67.9}B_{21.9}Si_{5.1}Nb_5Cu_{0.1}$. (For interpretation of the references to color in this figure legend, the reader is referred to the web version of this article.)

Table 1

Critical diameters D_c, mechanical properties (fracture strength σ_f and plastic strain ε_p), and magnetic properties (coercivity H_c and magnetic flux density at saturation B_s) of the as-cast $(Co_{0.7}Fe_{0.2}Ni_{0.1})_{68-x}B_{21.9}Si_{5.1}Nb_5Cu_x$ (x = 0, 0.1, 0.3, 0.5 and 0.7 at.%) metallic glasses.

Cu content	D_c (mm)	σ_f (MPa)	ε_p (%)	H_c (A/m)	B_s (T)
x = 0	5.0	4275	1.8	0.41	0.51
x = 0.1	4.0	4475	3.4	0.73	0.56
x = 0.3	3.5	4770	5.5	1.33	0.60
x = 0.5	3.0	4410	2.0	1.54	0.54
x = 0.7	2.0	4340	0.8	2.11	0.48

(III) CoFeBSiNb(Cu)(Ni). The BMGs in group I are CoTaB microalloying with Fe, Mo, Si or Cu, and no plasticity is reported for these BMGs. Besides, no BMG in this group simultaneously has satisfying GFA and large strength. For instance, the $Co_{42}Cu_1Fe_{20}Ta_{5.5}B_{26.5}Si_5$ BMG has the largest D_C (6 mm) in Co-based BMGs, but its strength is only 3928 MPa [15]; the $(Co_{0.535}Fe_{0.1}Ta_{0.055}B_{0.31})_{98}Mo_2$ BMG has a large strength of 5550 MPa but a small D_C of 1.5 mm [36]. The Co-based BMGs in group II are ternary Co-based alloys that have large fracture strength but limited GFA (less than 2 mm). The plastic strain of $Co_{57}Ta_8B_{35}$ and $Co_{59}Ta_6B_{35}$ are both below 2%, while their fracture strengths are extremely high, up to 5875 and 5720 MPa [14]. The $Co_{62}Nb_8B_{30}$ and $Co_{61}Nb_8B_{31}$ BMGs show large plasticity (2.9% and 5%), but lower fracture strength (5230 and 5290 MPa) [21,22]. For Co-based BMGs in group III, CoFeBSiNb BMG system shows excellent GFA up to 5.5 mm [10]. With minor addition of Cu, the plasticity of these BMGs is enlarged to 2.5%, while the fracture strength is among 4310–4370 MPa [20]. In this work, the $(Co_{0.7}Fe_{0.2}Ni_{0.1})_{67.7}B_{21.9}Si_{5.1}Nb_5Cu_{0.3}$ BMG prepared by co-adding Ni and Cu has the largest plastic strain (5.5%), high fracture strength (4770 MPa) and large GFA (3.5 mm), as indicated by a star in Fig. 2.

3.2. Dynamics of shear band

The macroscopic plastic deformation and fracture processes of BMGs are controlled by the evolution of shear bands, including initiation, propagation and interactions. It has been proved that the shear band dynamics can be reflected by serration flow from the stress-strain curves of compression tests [38–41]. Here, the stress-strain curves from the plastic deformation region for the $(Co_{0.7}Fe_{0.2}Ni_{0.1})_{68-x}B_{21.9}Si_{5.1}Nb_5Cu_x$ (x = 0 and 0.3 at.%) BMGs, which have typical different mechanical behaviors, are enlarged and shown in Figs. 3(a) and (b), respectively. The plastic deformation regions of both curves can be divided into two stages, including the steady plastic deformation stage (stage I) and the stress-decreasing stage (stage II). With the Cu content increasing from 0 to 0.3 at.%, the plastic strains at both stages increase. Besides, the shape of the serration patterns varies between the two BMGs. The stress vibrations for $(Co_{0.7}Fe_{0.2}Ni_{0.1})_{68}B_{21.9}Si_{5.1}Nb_5$ BMG is small at the beginning of the plastic deformation and increases continuously until failure, which reveals that the propagation of the shear bands is getting faster and close to the formation of cracks. By contrast, the serration of $(Co_{0.7}Fe_{0.2}Ni_{0.1})_{67.7}B_{21.9}Si_{5.1}Nb_5Cu_{0.3}$ BMG only has small complex vibrations without growing ones, indicating that the propagation of the shear bands in this alloy is quite stable [42].

The stress vibrations that are composed of repeated stress rising and drops have been observed on the stress-strain curves of compression and tension tests for both crystalline and amorphous materials. For crystalline materials, different mechanisms have been proposed to explain the stress vibrations, including phase transformation, slip avalanches, the interaction between dislocation motion and solute atoms diffusion [43,44]. For BMGs, as structural defects like dislocation or grain boundaries 'do not exist, it is well accepted that the stress rising process corresponds to the accumulation of the elastic strain energy, and the stress drop is related to the initiation and propagation of shear bands. Statistical analyses of the values of the stress drops help to further understand the shear band dynamics. The analyses of the serrations for the $(Co_{0.7}Fe_{0.2}Ni_{0.1})_{68-x}B_{21.9}Si_{5.1}Nb_5Cu_x$ (x = 0 and 0.3 at.%) BMGs are carried out by categorizing the values of stress drops into different ranges and counting the numbers of stress drops within each range, with the results shown in Fig. 3(c) and (d), respectively. The stress drops within the plastic deformation region of $(Co_{0.7}Fe_{0.2}Ni_{0.1})_{68}B_{21.9}Si_{5.1}Nb_5$ BMG follow Gaussian distribution (as indicated by the blue line), which means that the shear band dynamics in this BMG is in a chaotic state. In contrary, the stress drops of $(Co_{0.7}Fe_{0.2}Ni_{0.1})_{67.7}B_{21.9}Si_{5.1}Nb_5Cu_{0.3}$ BMG is in power-law distribution, revealing that the shear band dynamics in this BMG is a self-organized critical (SOC) behavior. BMGs that have SOC behavior are able to buffer against large stress and have high resistance to external impact, which means the matrix can endure more
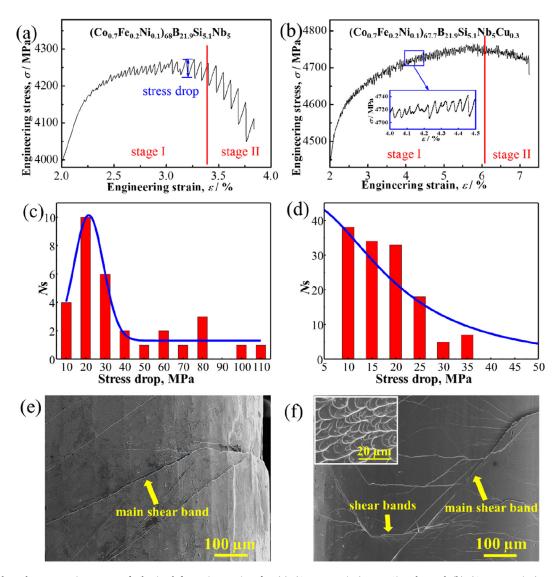
Fig. 3. The enlarged stress-strain curves of plastic deformation region for (a) $(Co_{0.7}Fe_{0.2}Ni_{0.1})_{68}B_{21.9}Si_{5.1}Nb_5$ and (b) $(Co_{0.7}Fe_{0.2}Ni_{0.1})_{67.7}B_{21.9}Si_{5.1}Nb_5Cu_{0.3}$ BMGs. The statistical distribution of stress drops counted from the continuous strain-stress curves for (c) $(Co_{0.7}Fe_{0.2}Ni_{0.1})_{68}B_{21.9}Si_{5.1}Nb_5$ and (d) $(Co_{0.7}Fe_{0.2}Ni_{0.1})_{67.7}B_{21.9}Si_{5.1}Nb_5Cu_{0.3}$ BMGs. SEM images of multiple shear bands on the outer surfaces of the (e) $(Co_{0.7}Fe_{0.2}Ni_{0.1})_{68}B_{21.9}Si_{5.1}Nb_5$ and (f) $(Co_{0.7}Fe_{0.2}Ni_{0.1})_{67.7}B_{21.9}Si_{5.1}Nb_5Cu_{0.3}$ glassy rods. The inset in (f) shows the vein patterns on the fracture surface of $(Co_{0.7}Fe_{0.2}Ni_{0.1})_{67.7}B_{21.9}Si_{5.1}Nb_5Cu_{0.3}$ glassy rod. (For interpretation of the references to color in this figure legend, the reader is referred to the web version of this article.)

deformation before fracture [45]. With 0 and 0.1 at.% Cu addition, the shear bands dynamics of the BMGs are in chaotic state, and change to SOC state with 0.3 at.% Cu addition, then back to chaotic state with 0.5 and 0.7 at.% Cu addition (data not shown), corresponding well with the plastic strain change of these BMGs.

The lateral surfaces of deformed $(Co_{0.7}Fe_{0.2}Ni_{0.1})_{68-x}B_{21.9}Si_{5.1}Nb_5Cu_x$ ($x = 0$ and 0.3 at.%) BMGs after compression tests were examined using SEM, as shown in Fig. 3(e) and (f), respectively. Several shear bands are formed on the Cu-free $(Co_{0.7}Fe_{0.2}Ni_{0.1})_{68}B_{21.9}Si_{5.1}Nb_5$ BMG. The prominent ones are approximately parallel to each other, and close to 45° to the loading direction, which is consistent with previous works [46]. Only a handful of shear band branching are visible on the surface after deformation. In contrary, multiple shear bands appear on the surface of deformed $(Co_{0.7}Fe_{0.2}Ni_{0.1})_{67.7}B_{21.9}Si_{5.1}Nb_5Cu_{0.3}$ BMG after compression test. The angle between the main shear band and the loading direction is also close to 45°. These shear bands intersect with each other, leading to the dissipation of elastic strain energy. As shown in the inset of Fig. 3(f), the fracture surface of the

$(Co_{0.7}Fe_{0.2}Ni_{0.1})_{67.7}B_{21.9}Si_{5.1}Nb_5Cu_{0.3}$ BMG exhibits well-developed vein patterns, which are characteristics of ductile BMGs [20,47].

The formation of multiple shear bands on the surface of BMGs reflect the SOC behavior of shear band dynamics during plastic deformation. Without Cu addition, when the deformation of the Co-based BMG is beyond the elastic limit, a few shear bands are initiated at the shear transformation zones and propagate through the alloy matrix quickly due to the rare occurrence of shear band interactions like branching, arresting, intersection or crossing, and then form cracks shortly. With proper addition of Cu, a larger number of shear bands are initiated, and their propagation is impeded due to the higher probability of shear band interactions, which also promotes the formation of multiple shear bands. As a result, the elastic strain energy is dissipated, leading to a stable shear band propagation process, which is defined as SOC behavior of serrations, and the catastrophic failure is avoided. Apparently, the minor Cu addition has a large impact on the shear band dynamics and thus on the mechanical behavior of the Co-based BMGs, and the reason for this will be discussed in Section 4.2.
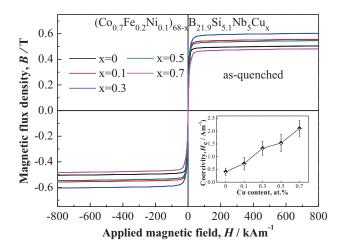
Fig. 4. Hysteresis loops for $(Co_{0.7}Fe_{0.2}Ni_{0.1})_{68-x}B_{21.9}Si_{5.1}Nb_5Cu_x$ ($x = 0$, 0.1, 0.3, 0.5 and 0.7 at.%) metallic glasses, with the corresponding H_c values shown in the inset (bottom right).

3.3. Magnetic properties

As the Co-based metallic glasses are potentially used as soft magnetic materials, it is important to maintain their good soft magnetic properties. The magnetic hysteresis loops of $(Co_{0.7}Fe_{0.2}Ni_{0.1})_{68-x}B_{21.9}Si_{5.1}Nb_5Cu_x$ ($x = 0$, 0.1, 0.3, 0.5 and 0.7 at.%) metallic glasses are shown in Fig. 4, with the H_c values shown in the inset. The values of B_s and H_c for the Co-based metallic glasses with different amount of Cu addition are also listed in Table 1. The B_s of this Co-based metallic glass system lies in a relatively high value range from 0.48 to 0.60 T. The B_s increase with increasing Cu content, reaching the maximum value (0.60 T) at $x = 0.3$, and then gradually decreases with further Cu addition. The H_c increases gradually from 0.41 to 2.11 A/m with the increase of Cu content. With 0.3 at.% Cu addition, the H_c is 1.33 A/m, which is very low for ferromagnetic metallic glasses. In a word, the $(Co_{0.7}Fe_{0.2}Ni_{0.1})_{67.7}B_{21.9}Si_{5.1}Nb_5Cu_{0.3}$ metallic glass also has excellent soft magnetic properties. The reason for the change of magnetic properties with Cu addition will be discussed at the end of Sections 4.1 and 4.2.

4. Discussion

4.1. Rearrangement of atoms with Cu addition

There is an obvious improvement of strength with 0.3 at.% Cu addition, which should be related to the structural evolution of these alloys. To unveil the origin of this strength improvement, the atomic structure of $(Co_{0.7}Fe_{0.2}Ni_{0.1})_{68-x}B_{21.9}Si_{5.1}Nb_5Cu_x$ ($x = 0$, 0.1, 0.3, 0.5 and 0.7 at.%) metallic glasses was analyzed using synchrotron XRD. The total structural factor $S(Q)$ as a function of the scattering vector Q of these samples were calculated and shown in Fig. 5(a). All of the plots show typical diffuse scattering patterns with oscillations extending up to 16 Å^{-1}, confirming the fully amorphous state of these samples. As Q is a reciprocal-space value, the diffuse maxima of $S(Q)$ with large Q values determine the short-range order (SRO) that are made of solute-centered quasi-equivalent clusters, while that with small Q values result from the medium-range order (MRO) which characterizes the packing and connection of the quasi-equivalent clusters [48]. The second maxima of all the samples are split into two, indicating a high degree of MRO for this alloy system. The first two maxima, which contain information about the MRO in these alloys, were fitted using pseudo-Voigt function and their peak positions (q_1 and q_2 as identified by the arrows) are summarized in Fig. 5(b). The position changes of the two peaks follow the same trend. When Cu content in the alloys increases from 0 to 0.3 at.%, q_1

and q_2 increase and reach the maximum values; by further increasing Cu content, the values of q_1 and q_2 decrease continuously. The absolute errors coming from fitting are much smaller than the changes of q_1 and q_2, ensuring the authenticity of results. However, the value of q_2/q_1 for the Co-based metallic glasses changes with the Cu contents, as shown in the inset of Fig. 5(b), indicating the influences of Cu addition on the interatomic distances at different levels of atomic shells are not the same. Based on the above results, the atoms in the medium- range for 0.3 at.% Cu-added alloy are likely to have a denser packing than other alloys prepared in this work, although the changes at different atomic shells are not the same.

To further investigate the structural evolution of these Co-based BMGs with Cu addition, the reduced pair correlation functions $G(r)$ of these alloys were calculated, as shown in Fig. 6. All curves oscillates around 0 Å^{-2} (i.e. $G(r) \rightarrow 0$ for $r \rightarrow \infty$). As $G(r)$ vs. r is in real-space, the function at small r range shows information about SRO, while that at large r range represents MRO structure. All of the curves show obvious oscillations up to $r \approx 25$ Å, indicating a high degree of MRO in this alloy system, which is consistent with the $S(q)$ analysis. The first peak contains information from the first coordination shell of atoms. As shown in the inset of Fig. 6(a), the first peak position r_1 (derived using pseudo-Voigt function fitting) decreases firstly as Cu content increases from 0 to 0.3 at.%, and then increases with further addition of Cu content up to 0.7 at.%. The absolute errors from fitting are less than 2.1%, which is within acceptance. The smallest r_1 for $(Co_{0.7}Fe_{0.2}Ni_{0.1})_{67.7}B_{21.9}Si_{5.1}Nb_5Cu_{0.3}$ metallic glass suggests that it has the most densely packed nearest-neighbors. Thus, based on the analyses of $S(q)$ and $G(r)$ functions, atoms in $(Co_{0.7}Fe_{0.2}Ni_{0.1})_{67.7}B_{21.9}Si_{5.1}Nb_5Cu_{0.3}$ metallic glass may be more densely packed in both short-range and medium-range scales than those in other alloys prepared in this work.

In order to unveil the origin of the dense packing, the changes of interatomic distances for the alloys are investigated. The possible nearest-neighbor atomic pairs and their theoretical bond lengths (r_{ij}) are obtained from the sum of atomic radii, which are 1.25, 1.24, 1.25, 0.83, 1.117, 1.43, and 1.28 Å for Co, Fe, Ni, B, Si, Nb, and Cu atoms, respectively. Other than the r_{ij}, the X-ray weighting factor (w_{ij}) at $q = 0$ Å^{-1}, which is closely related to the scattering power and concentration of the elements, is also calculated [49]. The values of r_{ij} and w_{ij} for $(Co_{0.7}Fe_{0.2}Ni_{0.1})_{68-x}B_{21.9}Si_{5.1}Nb_5Cu_x$ ($x = 0$, 0.1, 0.3, 0.5 and 0.7 at.%) metallic glasses are summarized in Table 2. The positions of different atomic pairs are labelled using dashed lines based on their bond lengths on the enlarged $G(r)$ curves (shifted vertically for comparison purposes) at the first coordination shell range, as shown in Fig. 6(b). Because it is difficult to distinguish the partial atomic pair correlations of Fe, Co, and Ni atoms due to their similar atomic radii, all of the three elements are defined as "M". Apparently, the small splits on the left of the plots are constructed by the atomic pairs containing metalloids, while the main first maxima is from the overlapping of partial atomic pair correlations between metallic elements, i.e. Fe, Co, Ni, Cu, and Nb. Furthermore, based on the values of w_{ij}, the dominant atomic pairs that constitute the first coordination shell are M-M and Co-Nb, as the w_{ij} of the remaining partials are negligible. Besides, with the increase of Cu contents, the overall contribution of M-M pairs decreases while that of the M-Cu pairs increases, and the contributions of the other atomic pairs remain almost the same. In other words, the shift of r_1 is mainly from the variations of atomic spacing between M-M and Co-Nb pairs, while the influence from the bond length of M-Cu pairs becomes more important with the increasing Cu content.

As the atomic radius of Cu is slightly larger than that of Fe, Co and Ni, the interatomic distances of the alloys should increase with Cu addition if we assume the atoms arrange in a hard-sphere model and only take the atomic radii into consideration, which is inconsistent with the above results. Thus, the interactions and influences between atoms, such as the mixing enthalpy, also play an important role in the rearrangement of the atoms with Cu addition. In these Co-based BMGs, the positive mix-
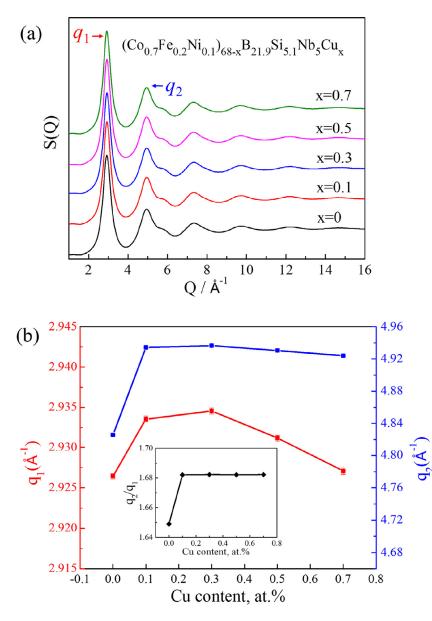
Fig. 5. (a) The synchrotron XRD total structural factor $S(q)$ of $(Co_{0.7}Fe_{0.2}Ni_{0.1})_{68-x}B_{21.9}Si_{5.1}Nb_5Cu_x$ (x = 0, 0.1, 0.3, 0.5 and 0.7 at.%) metallic glasses. (b) Change of the first and second diffuse maxima (q_1 and q_2) with Cu content.

ing enthalpy between the added Cu atoms and the major atoms, Fe-Cu (13 kJ/mol), Co-Cu (6 kJ/mol), Ni-Cu (4 kJ/mol) and Nb-Cu (3 kJ/mol) [25], results in mutual repulsion in these pairs. The change of bond lengths from the mutual repulsions between atoms in BMGs is not linear. On one hand, the spacing between Cu and Fe/ Co/ Ni/ Nb atomic pairs is enlarged with more Cu added. On the other hand, the Fe, Co, Ni, and Nb atoms are squeezed closer due to the repulsion force from Cu addition. With smaller amount of Cu, the squeezed spacing is larger than the enlarged portion. By further increasing the amount of Cu, the contribution of the enlarged bond length of M-Cu pairs becomes more prominent based on the w_{ij} results. And the enlargement between the atomic pairs with large mixing enthalpy can continue, but the squeezing is approaching a limit due to the sharply increased repulsive force between atoms with the decreasing atomic distance. Thus, the average atomic spacing increases again with more than 0.3 at.% Cu addition. This explains the lowest atomic spacing in $(Co_{0.7}Fe_{0.2}Ni_{0.1})_{67.7}B_{21.9}Si_{5.1}Nb_5Cu_{0.3}$ BMG. The decreased atomic spacing in metallic glasses means the space available for the atoms to move around their nearest neighbor without energy change is reduced [50]. Thus, larger driven force is needed for the movement of atoms, and the stress value before yielding is increased. From the macroscopic view, the strength of this Co-based

BMG is enhanced. This result is consistent with previous works, which reported the improved strength with reduced interatomic spacing in BMGs [51,52].

The changes of bond lengths with Cu addition also influence the magnetic properties of these Co-based metallic glasses, as the atomic magnetic moment is related to the number of the nearest ferromagnetic neighbors for Fe/Co/Ni atoms [53]. With addition of Cu content up to 0.3 at.%, the bonding between ferromagnetic atoms are promoted as revealed by the synchrotron XRD results, leading to the increase of the number of the nearest ferromagnetic neighbors for Fe, Co and Ni atoms [54]. Therefore, the B_s increases firstly with the increase of Cu content to 0.3 at.%. However, after adding more than a certain amount of Cu, the overall concentration of Fe, Co and Ni atoms is diluted, leading to the decrease of total number of magnetic moments in the alloys [55]. Thus, the B_s of the Co-based metallic glasses with 0.5 and 0.7 at.% Cu addition is then reduced.

4.2. Formation of crystal-like order regions in the amorphous matrix

The plasticity of BMGs usually decreases with reduced free volume, as smaller free volume provides less initiation sites and branch-
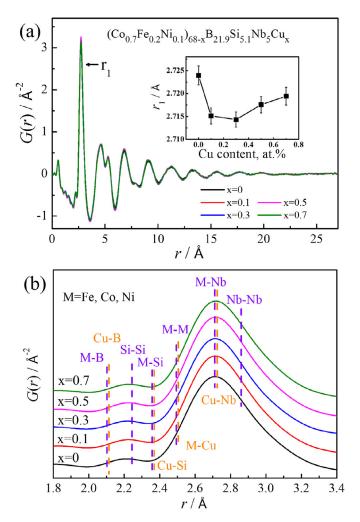
Table 2
The possible nearest-neighbor atomic pairs in $(Co_{0.7}Fe_{0.2}Ni_{0.1})_{68-x}$ $B_{21.9}Si_{5.1}Nb_5Cu_x$ ($x = 0$, 0.1, 0.3, 0.5 and 0.7 at.%) metallic glasses and their theoretical bond lengths r_{ij} and weighting factors w_{ij}.

Atomic pair ij	r_{ij}(Å)	$w_{ij\ x\ =\ =0}$	$w_{ij\ x\ =\ =0.1}$	$w_{ij\ x\ =\ =0.3}$	$w_{ij\ x\ =\ =0.5}$	$w_{ij\ x\ =\ =0.7}$
Co-Co	2.50	0.337	0.336	0.333	0.331	0.329
Co-Fe	2.49	0.185	0.185	0.184	0.182	0.181
Co-Ni	2.50	0.100	0.099	0.099	0.098	0.098
Fe-Fe	2.48	0.025	0.025	0.025	0.025	0.025
Fe-Ni	2.49	0.027	0.027	0.027	0.027	0.027
Ni-Ni	2.50	0.007	0.007	0.007	0.007	0.007
Co-B	2.08	0.057	0.057	0.057	0.057	0.057
Fe-B	2.07	0.016	0.016	0.016	0.016	0.016
Ni-B	2.08	0.008	0.008	0.008	0.008	0.008
Co-Si	2.37	0.037	0.037	0.037	0.037	0.037
Fe-Si	2.36	0.010	0.010	0.010	0.010	0.010
Ni-Si	2.37	0.006	0.006	0.006	0.005	0.005
Co-Nb	2.68	0.107	0.107	0.107	0.107	0.106
Fe-Nb	2.67	0.030	0.029	0.029	0.029	0.029
Ni-Nb	2.68	0.016	0.016	0.016	0.016	0.016
Co-Cu	2.53	–	0.002	0.005	0.008	0.011
Fe-Cu	2.52	–	0.000	0.001	0.002	0.003
Ni-Cu	2.53	–	0.000	0.001	0.001	0.002
B-B	1.66	0.002	0.002	0.002	0.002	0.002
B-Si	1.95	0.003	0.003	0.003	0.003	0.003
B-Nb	2.26	0.009	0.009	0.009	0.009	0.009
B-Cu	2.11	–	0.000	0.000	0.001	0.001
Si-Si	2.23	0.001	0.001	0.001	0.001	0.001
Si-Nb	2.55	0.006	0.006	0.006	0.006	0.006
Si-Cu	2.40	–	0.000	0.000	0.000	0.001
Nb-Nb	2.86	0.009	0.009	0.009	0.009	0.009
Nb-Cu	2.71	–	0.000	0.001	0.001	0.002
Cu-Cu	2.56	–	0.000	0.000	0.000	0.000

Fig. 6. (a) The reduced pair correlation functions $G(r)$ of $(Co_{0.7}Fe_{0.2}Ni_{0.1})_{68-x}B_{21.9}Si_{5.1}Nb_5Cu_x$ ($x = 0$, 0.1, 0.3, 0.5 and 0.7 at.%) metallic glasses. The inset shows the variation of the first peak position (r_1) with Cu content. (b) The reduced pair correlation functions $G(r)$ of $(Co_{0.7}Fe_{0.2}Ni_{0.1})_{68-x}B_{21.9}Si_{5.1}Nb_5Cu_x$ ($x = 0$, 0.1, 0.3, 0.5 and 0.7 at.%) metallic glasses depicted in the range of the first coordination shell (shifted curves). The dashed lined shows the positions of the possible nearest-neighbor atomic pairs, with the ones containing Cu in orange and others in purple. (For interpretation of the references to color in this figure legend, the reader is referred to the web version of this article.)

ing for shear bands. However, this is not the case in this work. $(Co_{0.7}Fe_{0.2}Ni_{0.1})_{67.7}B_{21.9}Si_{5.1}Nb_5Cu_{0.3}$ BMG has the smallest amount of atomic spacing, which means it has the least free volume, but its plastic strain is the largest. To uncover the reason of this contradiction, HRTEM analysis was performed on $(Co_{0.7}Fe_{0.2}Ni_{0.1})_{68-x}Si_{5.1}Nb_5Cu_x$ ($x = 0$ and 0.3 at.%) BMGs using spherical aberration TEM to clearly compare the nanostructural change with Cu addition. The representative HRTEM images of these two BMGs are shown in Fig. 7(a) and (b), with the corresponding selected area electron diffraction patterns (SAED) shown in the insets. As no crystallites or sharp diffraction rings are observed, the amorphous features of the samples with or without Cu addition can be confirmed. In order to obtain the atomic configuration of the BMGs more clearly, the FFT filtered HRTEM images of the selected regions (the white squares) in Fig. 7(a) and (b) are shown in Fig. 8(a) and (b), respectively. Within the current visual field in Fig. 8(a), most areas of the $(Co_{0.7}Fe_{0.2}Ni_{0.1})_{68}B_{21.9}Si_{5.1}Nb_5$ BMG are composed of disordered structures. Some atom-centered clusters (highlighted by the yellow circles), indicating SRO regions, are also observed in the matrix [56]. Besides, the FFT of the area in this whole image, as shown in the inset of Fig. 8(a), reveals the disorder structure of this sample.

In contrary, with only 0.3 at.% Cu addition, the atomic structure of $(Co_{0.7}Fe_{0.2}Ni_{0.1})_{67.7}B_{21.9}Si_{5.1}Nb_5Cu_{0.3}$ BMG seems to be more ordered. Other than the SRO regions highlighted by the yellow circles, the crystal-like order (CLO) regions of ~1–2 nm in size with lattice fringes that have imperfect 3D translational symmetry appear in the matrix (highlighted by the yellow squares) [57]. As shown in the inset of Fig. 8(b), two pairs of diffraction spots (indicated by the white circles) appear in the FFT of the representative CLO region (region D), which further confirm the CLO in this region. Although the FFT image shows that this HRTEM has some astigmatism, it doesn't affect the confirmation of existence of the SRO and CLO structures in this sample. As these kinds of CLO regions are rarely observed in the $(Co_{0.7}Fe_{0.2}Ni_{0.1})_{68}B_{21.9}Si_{5.1}Nb_5$ BMG, these CLO regions are believed to be induced by minor Cu addition due to the large mixing enthalpy between Co-Cu, Fe-Cu, Ni-Cu, and Nb-Cu atomic pairs.

Furthermore, in order to statistically compare the structural disordering degree of the $(Co_{0.7}Fe_{0.2}Ni_{0.1})_{68-x}B_{21.9}Si_{5.1}Nb_5Cu_x$ ($x = 0$ and 0.3 at.%) BMGs, the areal fraction of the CLO regions are calculated by analyzing the 2D auto-correlation transformation of the divided cells (1.995 nm x 1.995 nm) for the two BMGs, as shown in Fig. 9. The size of each cell is close to that of the CLO region observed in Fig. 8(b). If the auto-correlated pattern of the cell shows translational symmetry, as for example the cell at the 2nd row and 2nd column of Fig. 9(a), it is considered to be a CLO region [57]. If the auto-correlation shows maze-like pattern, as for example the cell at the 1st row and 1st column of Fig. 9(b), the area is considered to be disordered. With this criteria, different regions of the $(Co_{0.7}Fe_{0.2}Ni_{0.1})_{68-x}B_{21.9}Si_{5.1}Nb_5Cu_x$ ($x = 0$ and 0.3 at.%) BMGs are analyzed, and the representative ones are shown in Figs. 9(a) and (b), respectively. According to the statistics, the areal fraction of CLO regions in the Co-based BMG without Cu addition is 11.5 ± 1.5%, and increases distinctly to 24.3 ± 1.2% in $(Co_{0.7}Fe_{0.2}Ni_{0.1})_{67.7}B_{21.9}Si_{5.1}Nb_5Cu_{0.3}$ BMG. Apparently, the local structural ordering is improved with Cu addition.

The increased structural ordering, i.e. the formation of CLO regions, is mostly due to the large positive mixing enthalpy between Cu
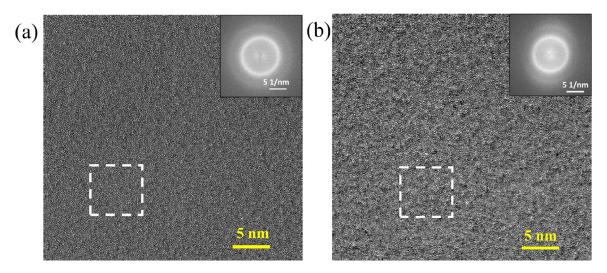
Fig. 7. HRTEM images and corresponding SAED patterns of (a) $(Co_{0.7}Fe_{0.2}Ni_{0.1})_{68}B_{21.9}Si_{5.1}Nb_5$ and (b) $(Co_{0.7}Fe_{0.2}Ni_{0.1})_{67.7}B_{21.9}Si_{5.1}Nb_5Cu_{0.3}$ BMGs.
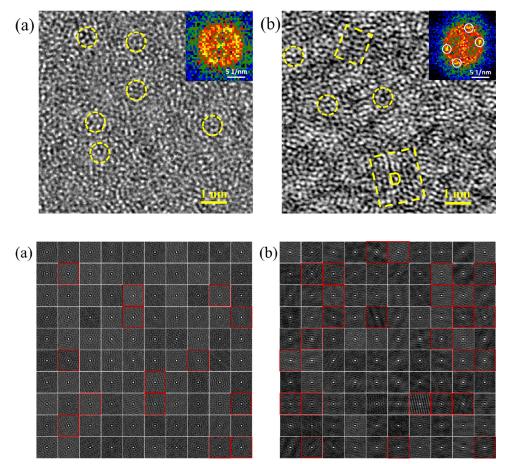

Fig. 8. The FFT filtered patterns of (a) $(Co_{0.7}Fe_{0.2}Ni_{0.1})_{68}B_{21.9}Si_{5.1}Nb_5$ and (b) $(Co_{0.7}Fe_{0.2}Ni_{0.1})_{67.7}B_{21.9}Si_{5.1}Nb_5Cu_{0.3}$ BMGs, with corresponding insets showing the FFT patterns.

Fig. 9. The representative 2D auto-correlated transformation of divided cells for the HRTEM images taken from (a) $(Co_{0.7}Fe_{0.2}Ni_{0.1})_{68}B_{21.9}Si_{5.1}Nb_5$ and (b) $(Co_{0.7}Fe_{0.2}Ni_{0.1})_{67.7}B_{21.9}Si_{5.1}Nb_5Cu_{0.3}$ BMGs.

and Co/Fe/Ni atomic pairs. The repulsive force between Cu and the ferromagnetic atoms results in the formation of the Co(Fe,Ni)- rich and Co(Fe,Ni)- poor regions during quenching, promoting the more ordered arrangements of atoms and the formation of CLO regions. The CLO regions of ~1–2 nm in size are not large enough to be detected by XRD, and will not' change the overall amorphous state of the sample. However, these increased structural ordering of the BMGs plays an important role during plastic deformation [58,59]. When $(Co_{0.7}Fe_{0.2}Ni_{0.1})_{67.7}B_{21.9}Si_{5.1}Nb_5Cu_{0.3}$ BMG is under loading, the CLO regions act as the initiation sites for shear bands, and also intersect with the shear bands during their propagation to induce the formation of multiple shear bands. The shear bands interact with each other during compression tests, which leads to the macroscopically stable serration flow behavior of this BMG. The large elastic energy is dissipated by the initiation and propagation of shear bands. As a result, although the 0.3 at.% Cu-added BMG has the lowest free volume, the CLO regions in this BMG enhance its plasticity successfully. Nevertheless, when the Cu content is up to 0.7 at.%, not only α-(Fe, Co, Ni) appear, but also large size (Fe, Co, Ni)$_{23}$B$_6$ and (Fe, Co, Ni)$_2$B crystalline phases and aggregates are precipitated, as shown in Fig. 10, which are not suitable for interaction with shear bands, and thus the plasticity of the alloy is deteriorated.
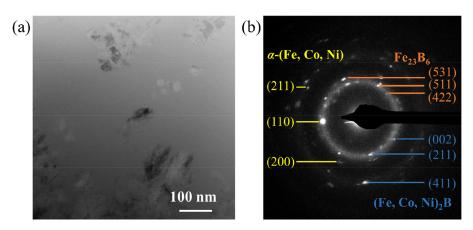
Fig. 10. The representative (a) TEM image and (b) SAED pattern of $(Co_{0.7}Fe_{0.2}Ni_{0.1})_{67.3}B_{21.9}Si_{5.1}Nb_5Cu_{0.7}$ BMG.

Also, both the formation of CLO structures in 0.3 at.% Cu-added alloy, and the large crystals in 0.7 at.% Cu-added alloy can lead to the pinning of magnetic domain, which results in the increase of H_c. This explains the continuous increase of H_c values for the Co-based metallic glasses prepared in this work with the increasing amount of Cu addition, as shown in Fig. 4.

5. Conclusions

In conclusion, a novel $(Co_{0.7}Fe_{0.2}Ni_{0.1})_{67.7}B_{21.9}Si_{5.1}Nb_5Cu_{0.3}$ BMG with a high fracture strength of 4770 MPa and a large plastic strain of 5.5% is successfully developed. The enhanced strength of $(Co_{0.7}Fe_{0.2}Ni_{0.1})_{67.7}B_{21.9}Si_{5.1}Nb_5Cu_{0.3}$ BMG is attributed to the reduced average atomic spacing with Cu addition. The plasticity of this BMG is improved by the existence of CLO regions in the amorphous matrix in despite of the reduced free volume. The $(Co_{0.7}Fe_{0.2}Ni_{0.1})_{67.7}B_{21.9}Si_{5.1}Nb_5Cu_{0.3}$ BMG also shows good soft magnetic properties. The decreased atomic spacing between ferromagnetic atoms improves the saturation magnetization to 0.60 T, while the coercivity is slightly increased (but still as low as 1.33 A/m) due to the pinning effect at CLO regions. This work provides a guideline in obtaining Co-based BMGs with good GFA, high strength, large room-temperature plasticity, as well as satisfying soft magnetic properties.

Declaration of Competing Interest

The authors declare that they have no known competing financial interests or personal relationships that could have appeared to influence the work reported in this paper.

Acknowledgements

Supplementary materials

Supplementary material associated with this article can be found, in the online version, at doi:10.1016/j.mtla.2019.100561.

References

[1] R.C. Ohandley, Magnetic-moments and electronic-structure of Co-base metallic glasses, Solid State Commun. 38 (8) (1981) 703–708.

[2] J. Degro, P. Vojtanik, J. Filipensky, P. Duhaj, Influence of thermal-treatment on the magnetic-properties of Co-based and Fe-based amorphous-alloys, J. Magn. Magn. Mater. 117 (1–2) (1992) 251–258.

[3] P.T. Squire, D. Atkinson, M.R.J. Gibbs, S. Atalay, Amorphous wires and their applications, J. Magn. Magn. Mater. 132 (1–3) (1994) 10–21.

[4] A. Inoue, A. Katsuya, Multicomponent Co-based amorphous alloys with wide supercooled liquid region, Mater. Trans. JIM 37 (6) (1996) 1332–1336.

[5] G. Bordin, G. Buttino, A. Cecchetti, M. Poppi, Temperature dependence of magnetic properties of a Co-based alloy in amorphous and nanostructured phase, J. Magn. Magn. Mater. 195 (3) (1999) 583–587.

[6] A. Inoue, B.L. Shen, H. Koshiba, H. Kato, A.R. Yavari, Cobalt-based bulk glassy alloy with ultrahigh strength and soft magnetic properties, Nat. Mater. 2 (10) (2003) 661–663.

[7] A. Inoue, B.L. Shen, H. Koshiba, H. Kato, A.R. Yavari, Ultra-high strength above 5000MPa and soft magnetic properties of Co-Fe-Ta-B bulk glassy alloys, Acta Mater. 52 (6) (2004) 1631–1637.

[8] C.T. Chang, B.L. Shen, A. Inoue, Co-Fe-B-Si-Nb bulk glassy alloys with superhigh strength and extremely low magnetostriction, Appl. Phys. Lett. 88 (1) (2006).

[9] K. Amiya, A. Urata, N. Nishiyama, A. Inoue, Magnetic properties of Co-Fe-B-Si-Nb bulk glassy alloy with zero magnetostriction, J. Appl. Phys. 101 (9) (2007).

[10] Y.Q. Dong, A.D. Wang, Q.K. Man, B.L. Shen, $(Co_{1-x}Fe_x)_{68}B_{21.9}Si_{5.1}Nb_5$ bulk glassy alloys with high glass-forming ability, excellent soft-magnetic properties and superhigh fracture strength, Intermetallics 23 (2012) 63–67.

[11] A.H. Taghvaei, M. Stoica, K.G. Prashanth, J. Eckert, Fabrication and characterization of bulk glassy $Co_{40}Fe_{22}Ta_8B_{30}$ alloy with high thermal stability and excellent soft magnetic properties, Acta Mater. 61 (17) (2013) 6609–6621.

[12] Y.Y. Cheng, C. Chen, M.J. Shi, T. Zhang, Synthesis of CoCrMoCB bulk metallic glasses with high strength and good plasticity via regulating the metalloid content, J. Non-Cryst. Solids 410 (2015) 155–159.

[13] L.Y. Bie, Q. Li, D. Cao, H.X. Li, J.J. Zhang, C.T. Chang, Y.F. Sun, Preparation and properties of quaternary CoMoPB bulk metallic glasses, Intermetallics 71 (2016) 7–11.

[14] J.F. Wang, R. Li, N.B. Hua, T. Zhang, Co-based ternary bulk metallic glasses with ultrahigh strength and plasticity, J. Mater. Res. 26 (16) (2011) 2072–2079.

[15] Z.O. Yazici, A. Hitit, Y. Yalcin, M. Ozgul, Effects of minor Cu and Si additions on glass forming ability and mechanical properties of Co-Fe-Ta-B bulk metallic glass, Met. Mater. Int. 22 (1) (2016) 50–57.

[16] Y.Q. Cheng, A.J. Cao, E. Ma, Correlation between the elastic modulus and the intrinsic plastic behavior of metallic glasses: the roles of atomic configuration and alloy composition, Acta Mater. 57 (11) (2009) 3253–3267.

[17] Z.Q. Liu, W.H. Wang, M.Q. Jiang, Z.F. Zhang, Intrinsic factor controlling the deformation and ductile-to-brittle transition of metallic glasses, Phil. Mag. Lett. 94 (10) (2014) 658–668.

[18] M. Stoica, S. Scudino, J. Bednarcik, I. Kaban, J. Eckert, FeCoSiBNbCu bulk metallic glass with large compressive deformability studied by time-resolved synchrotron X-ray diffraction, J. Appl. Phys. 115 (5) (2014).

[19] M. Stoica, P. Ramasamy, I. Kaban, S. Scudino, M. Nicoara, G.B.M. Vaughan, J. Wright, R. Kumar, J. Eckert, Structure evolution of soft magnetic $(Fe_{36}Co_{36}B_{19.2}Si_{4.8}Nb_4)_{100-x}Cu_x$ (x=0 and 0.5) bulk glassy alloys, Acta Mater. 95 (2015) 335–342.

[20] G.L. Zhang, Q.Q. Wang, C.C. Yuan, W.M. Yang, J. Zhou, L. Xue, F. Hu, B.A. Sun, B.L. Shen, Effects of cu additions on mechanical and soft-magnetic properties of CoFeBSiNb bulk metallic glasses, J. Alloys Compd. 737 (2018) 815–820.

[21] C.C. Dun, H.S. Liu, B.L. Shen, Enhancement of plasticity in Co-Nb-B Ternary bulk metallic glasses with ultrahigh strength, J. Non-Cryst. Solids 358 (23) (2012) 3060–3064.

[22] C.C. Dun, H.S. Liu, L. Hou, L. Xue, L.T. Dou, W.M. Yang, Y.C. Zhao, B.L. Shen, Ductile Co-Nb-B bulk metallic glass with ultrahigh strength, J. Non-Cryst. Solids 386 (2014) 121–123.

[23] C.C. Yuan, Z.W. Lv, C.M. Pang, X.L. Wu, S. Lan, C.Y. Lu, L.G. Wang, H.B. Yu, J.H. Luan, W.W. Zhu, G.L. Zhang, Q. Liu, X.L. Wang, B.L. Shen, Atomic-scale heterogeneity in large-plasticity Cu-doped metallic glasses, J. Alloys Compd. 798 (2019) 517–522.

[24] A. Takeuchi, A. Inoue, Classification of bulk metallic glasses by atomic size difference, heat of mixing and period of constituent elements and its application to characterization of the main alloying element, Mater. Trans. 46 (12) (2005) 2817–2829.

[25] E.S. Park, D.H. Kim, Phase separation and enhancement of plasticity in Cu-Zr-Al-Y bulk metallic glasses, Acta Mater. 54 (10) (2006) 2597–2604.

[26] H.K. Kim, M. Lee, K.R. Lee, J.C. Lee, How can a minor element added to a binary amorphous alloy simultaneously improve the plasticity and glass-forming ability? Acta Mater. 61 (17) (2013) 6597–6608.

[27] H.K. Kim, J.P. Ahn, B.J. Lee, K.W. Park, J.C. Lee, Role of atomic-scale chemical heterogeneities in improving the plasticity of Cu-Zr-Ag bulk amorphous alloys, Acta Mater. 157 (2018) 209–217.

[28] S.F. Guo, J.L. Qiu, P. Yu, S.H. Xie, W. Chen, Fe-based bulk metallic glasses: brittle or ductile? Appl. Phys. Lett. 105 (16) (2014) 161901.

[29] W.M. Yang, H.S. Liu, Y.C. Zhao, A. Inoue, K.M. Jiang, J.T. Huo, H.B. Ling, Q. Li, B.L. Shen, Mechanical properties and structural features of novel Fe-based bulk metallic glasses with unprecedented plasticity, Sci. Rep.-Uk 4 (2014) 6233.

[30] B. Sarac, Y.P. Ivanov, A. Chuvilin, T. Schoberl, M. Stoica, Z.L. Zhang, J. Eckert, Origin of large plasticity and multiscale effects in iron-based metallic glasses, Nat. Commun. 9 (2018) 1333.

[31] R.M. Niu, K. Han, Cross-section metal sample preparations for transmission electron microscopy by electro-deposition and electropolishing, Microsc. Res. Techniq. 76 (5) (2013) 476–480.

[32] A. Frank, R. Changizi, C. Scheu, Challenges in TEM sample preparation of solvothermally grown CuInS$_2$ films, Micron 109 (2018) 1–10.

[33] A.P. Hammersley, S.O. Svensson, M. Hanfland, A.N. Fitch, D. Hausermann, Two-dimensional detector software: from real detector to idealised image or two-theta scan, High Press. Res. 14 (4–6) (1996) 235–248.

[34] I.K. Jeong, J. Thompson, T. Proffen, A.M.P. Turner, S.J.L. Billinge, PDFgetX: a program for obtaining the atomic pair distribution function from X-ray powder diffraction data, J. Appl. Crystallogr. 34 (2001) 536.

[35] X.Y. Qiu, J.W. Thompson, S.J.L. Billinge, PDFgetX2: a GUI-driven program to obtain the pair distribution function from X-ray powder diffraction data, J. Appl. Crystallogr. 37 (2004).

[36] B.L. Shen, A. Inoue, Enhancement of the fracture strength and glass-forming ability of CoFeTaB bulk glassy alloy, J. Phys-Condens. Mat. 17 (37) (2005) 5647–5653.

[37] C.L. Zhu, Q. Wang, Y.M. Wang, J.B. Qiang, C. Dong, Co-B-Si-Ta bulk metallic glasses designed using cluster line and alloying, J. Alloys Compd. 504 (2010) S34–S37.

[38] R. Sarmah, G. Ananthakrishna, B.A. Sun, W.H. Wang, Hidden order in serrated flow of metallic glasses, Acta Mater. 59 (11) (2011) 4482–4493.

[39] F. Haag, D. Beitelschmidt, J. Eckert, K. Durst, Influences of residual stresses on the serrated flow in bulk metallic glass under elastostatic four-point bending - A nanoindentation and atomic force microscopy study, Acta Mater. 70 (2014) 188–197.

[40] H.B. Ke, B.A. Sun, C.T. Liu, Y. Yang, Effect of size and base-element on the jerky flow dynamics in metallic glass, Acta Mater. 63 (2014) 180–190.

[41] Z. Wang, J.W. Qiao, H. Tian, B.A. Sun, B.C. Wang, B.S. Xu, M.W. Chen, Composition mediated serration dynamics in Zr-based bulk metallic glasses, Appl. Phys. Lett. 107 (20) (2015) 201902.

[42] B.A. Sun, W.H. Wang, The fracture of bulk metallic glasses, Prog. Mater. Sci. 74 (2015) 211–307.

[43] J. Antonaglia, X. Xie, Z. Tang, C.W. Tsai, J.W. Qiao, Y. Zhang, M.O. Laktionova, E.D. Tabachnikova, J.W. Yeh, O.N. Senkov, M.C. Gao, J.T. Uhl, P.K. Liaw, K.A. Dahmen, Temperature effects on deformation and serration behavior of high-entropy alloys (HEAs), JOM-Us 66 (10) (2014) 2002–2008.

[44] K. Han, Y. Xin, R. Walsh, S. Downey, P.N. Kalu, The effects of grain boundary precipitates on cryogenic properties of aged 316-type stainless steels, Mat. Sci. Eng. A-Struct. 516 (1–2) (2009) 169–179.

[45] B.A. Sun, S. Pauly, J. Tan, M. Stoica, W.H. Wang, U. Kuhn, J. Eckert, Serrated flow and stick-slip deformation dynamics in the presence of shear-band interactions for a Zr-based metallic glass, Acta Mater. 60 (10) (2012) 4160–4171.

[46] J. Zhou, W.M. Yang, C.C. Yuan, B.A. Sun, B.L. Shen, Ductile FeNi-based bulk metallic glasses with high strength and excellent soft magnetic properties, J. Alloys Compd. 742 (2018) 318–324.

[47] M.Q. Jiang, Z. Ling, J.X. Meng, L.H. Dai, Energy dissipation in fracture of bulk metallic glasses via inherent competition between local softening and quasi-cleavage, Philos. Mag. 88 (3) (2008) 407–426.

[48] A.H. Taghvaei, H.S. Shahabi, J. Bednarcik, J. Eckert, Fabrication and characterization of Co$_{40}$Fe$_{22}$Ta$_{8-x}$Y$_x$B$_{30}$ (x=0, 2.5, 4, 6, and 8) metallic glasses with high thermal stability and good soft magnetic properties, J. Appl. Phys. 116 (18) (2014) 184904.

[49] M. Stoica, J. Das, J. Bednarcik, H. Franz, N. Mattern, W.H. Wang, J. Eckert, Strain distribution in Zr$_{64.13}$Cu$_{15.75}$Ni$_{10.12}$Al$_{10}$ bulk metallic glass investigated by in situ tensile tests under synchrotron radiation, J. Appl. Phys. 104 (1) (2008) 013522.

[50] M.H. Cohen, D. Turnbull, Molecular transport in liquids and glasses, J. Chem. Phys. 31 (5) (1959) 1164–1169.

[51] C.C. Dun, H.S. Liu, B.L. Shen, Enhancement of plasticity in Co-Nb-B ternary bulk metallic glasses with ultrahigh strength, J. Non-Cryst. Solids 358 (23) (2012) 3060–3064.

[52] Y. Wu, H. Wang, Y.Q. Cheng, X.J. Liu, X.D. Hui, T.G. Nieh, Y.D. Wang, Z.P. Lu, Inherent structure length in metallic glasses: simplicity behind complexity, Sci. Rep.-Uk 5 (2015) 12137.

[53] F.E. Luborsky, in: F.E. Luborsky (Ed.), Amorphous Metallic Alloys, Butterworth-Heinemann, 1983, pp. 360–380.

[54] Z.B. Jiao, H.X. Li, J.E. Gao, Y. Wu, Z.P. Lu, Effects of alloying elements on glass formation, mechanical and soft-magnetic properties of Fe-based metallic glasses, Intermetallics 19 (10) (2011) 1502–1508.

[55] L.T. Dou, H.S. Liu, L. Hou, L. Xue, W.M. Yang, Y.C. Zhao, C.T. Chang, B.L. Shen, Effects of Cu substitution for Fe on the glass-forming ability and soft magnetic properties for Fe-based bulk metallic glasses, J. Magn. Magn. Mater. 358 (2014) 23–26.

[56] W.M. Yang, H.S. Liu, X.J. Liu, G.X. Chen, C.C. Dun, Y.C. Zhao, Q.K. Man, C.T. Chang, B.L. Shen, A. Inoue, R.W. Li, J.Z. Jiang, Correlation of atomic packing with the boson peak in amorphous alloys, J. Appl. Phys. 116 (12) (2014) 123512.

[57] Q. Wang, C.T. Liu, Y. Yang, J.B. Liu, Y.D. Dong, J. Lu, The atomic-scale mechanism for the enhanced glass-forming-ability of a Cu-Zr based bulk metallic glass with minor element additions, Sci. Rep.-Uk 4 (2014) 4648.

[58] P.Y. Zhao, J. Li, J. Hwang, Y.Z. Wang, Influence of nanoscale structural heterogeneity on shear banding in metallic glasses, Acta Mater. 134 (2017) 104–115.

[59] J.C. Qiao, Q. Wang, J.M. Pelletier, H. Kato, R. Casalini, D. Crespo, E. Pineda, Y. Yao, Y. Yang, Structural heterogeneities and mechanical behavior of amorphous alloys, Prog. Mater. Sci. 104 (2019) 250–329.